PTEP

Prog. Theor. Exp. Phys. **2014**, 073D01 (11 pages)
DOI: 10.1093/ptep/ptu086

Deformation and α clustering in excited states of ^{42}Ca

Yasutaka Taniguchi 谷口億宇[1,2,3,*]

[1]*Center for Computational Sciences, University of Tsukuba, Tsukuba, Ibaraki 305-8577, Japan*
[2]*RIKEN Nishina Center for Accelerator-Based Science, Wako, Saitama 351-0198, Japan*
[3]*Present address: Department of Medical and General Sciences, Nihon Institute of Medical Science, Moroyama-machi, Iruma-gun, Saitama 350-0435, Japan*
*E-mail: yasutaka@nims.ac.jp

Received April 10, 2014; Revised May 13, 2014; Accepted May 21, 2014; Published July 1, 2014

The coexistence of various low-lying deformed states in ^{42}Ca and the α–^{38}Ar correlations in those deformed states have been investigated using deformed-basis antisymmetrized molecular dynamics. Wave functions of the low-lying states are obtained via parity and angular momentum projections and the generator coordinate method (GCM). Basis wave functions of the GCM calculation are obtained via energy variations with constraints on the quadrupole deformation parameter β and the distance between α and the ^{38}Ar clusters. The rotational bands built on the $J^\pi = 0^+_2$ (1.84 MeV) state as well as the $J^\pi = 0^+_3$ (3.30 MeV) state are both reproduced. The coexistence of two additional $K^\pi = 0^+$ rotational bands is predicted; one band is shown to be built on the $J^\pi = 0^+_3$ state. Members of the ground-state band and the rotational band built on the $J^\pi = 0^+_3$ state contain α–^{38}Ar cluster structure components.

Subject Index D13

1. Introduction

Drastic structural changes initiated by low excitation energies are a significant characteristic of nuclear systems, and the coexistence of deformed states and cluster structures is a typical phenomenon. In the mass number region $A \sim 40$, low-lying normal-deformed (ND) and superdeformed (SD) bands with many-particle–many-hole (mp–mh) configurations have been confirmed experimentally in ^{36,38,40}Ar [1–3], ^{40}Ca [4], ^{42}Ca [5,6], and ^{44}Ti [7]. The SD band in ^{36}Ar, ND and SD bands in ^{40}Ca, and SD band in ^{44}Ti are considered to have configurations of $4p8h$, $4p4h$, $8p8h$, and $8p4h$, respectively, relative to the sd-shell double-closed structure. Coupling of the cluster structure components in deformed states such as the α-cluster structure in the ND band of ^{40}Ca [8–11] and the ground-state band in ^{44}Ti [8,9,12] has also been investigated.

In ^{42}Ca, deformed states with mp–mh configurations and clustering behavior have been observed experimentally, and the rotational band built on the $J^\pi = 0^+_2$ (1.84 MeV) state ($K^\pi = 0^+_2$ band) has been observed [5,6]. This rotational band has a large moment of inertia that is similar to those of the SD bands in ^{36}Ar and ^{40}Ca, scaled by $A^{5/3}$ [6], which is proportional to the square of the quadrupole deformation parameter β in the liquid-drop model. In contrast to the small level spacings, the in-band E2 transition strengths are rather weak and are of the same order as those of the ND band in ^{40}Ca. With regard to α-cluster structures, strong population to the $J^\pi = 0^+_1$ and 0^+_3 (3.30 MeV)

states has been observed in α-transfer reactions to ^{38}Ar, and the ratios of the cross sections of α and $2n$ transfer reactions suggest that the $J^\pi = 0_2^+$ and 0_3^+ states have configurations of $6p4h$ and $4p2h$, respectively [13]. Theoretically, the $\alpha + {}^{38}$Ar orthogonality condition model (OCM) describes $4p2h$ states with α–^{38}Ar cluster structures, but a rotational band with a $6p4h$ configuration is not obtained in low-lying states [14]. To understand the structures in ^{42}Ca, various deformations with mp–mh configurations and clustering should be taken into account, but such a study has never been performed. The structures of low-lying states in ^{42}Ca have not yet been clarified.

This paper aims to clarify the structures of excited deformed bands in positive-parity states of ^{42}Ca by focusing on the coexistence of rotational bands with mp–mh configurations. The α–^{38}Ar cluster correlations in low-lying deformed states are also discussed. To discuss the coexistence and mixing of deformed and cluster structures, the generator coordinate method (GCM) is used.

This paper is organized as follows: In Sect. 2, the framework of this study is explained briefly. In Sect. 3, the results of energy variation to obtain the GCM basis are shown. In Sect. 4, the coexistence of various deformed states and their structures are discussed. In Sect. 5, the relations between E2 transition strengths and particle–hole configurations are discussed. Finally, conclusions are given in Sect. 6.

2. Framework

In this section, the framework of the study is explained briefly. Details of the framework are provided in Refs. [15–17].

2.1. *Wave function*

The wave functions in low-lying states are obtained by using the parity and angular momentum projection (AMP) and the GCM with deformed-basis antisymmetrized molecular dynamics (AMD) wave functions. A deformed-basis AMD wave function $|\Phi\rangle$ is a Slater determinant of Gaussian wave packets that can deform triaxially such that

$$|\Phi\rangle = \hat{\mathcal{A}}|\varphi_1, \varphi_2, \ldots, \varphi_A\rangle, \tag{1}$$

$$|\varphi_i\rangle = |\phi_i\rangle \otimes |\chi_i\rangle \otimes |\tau_i\rangle, \tag{2}$$

$$\langle \mathbf{r}|\phi_i\rangle = \pi^{-3/4}(\det \mathsf{K})^{1/2} \exp\left[-\frac{1}{2}(\mathsf{K}\mathbf{r} - \mathbf{Z}_i)^2\right], \tag{3}$$

$$|\chi_i\rangle = \chi_i^{\uparrow}|\uparrow\rangle + \chi_i^{\downarrow}|\downarrow\rangle, \tag{4}$$

$$|\tau_i\rangle = |\pi\rangle \text{ or } |\nu\rangle, \tag{5}$$

where $\hat{\mathcal{A}}$ denotes the antisymmetrization operator, and $|\varphi_i\rangle$ denotes a single-particle wave function. $|\phi_i\rangle$, $|\chi_i\rangle$, and $|\tau_i\rangle$ denote the spatial, spin, and isospin components, respectively, of each single-particle wave function $|\varphi_i\rangle$. The real 3×3 matrix K denotes the width of the Gaussian single-particle wave functions that can deform triaxially, which is common to all nucleons. The $\mathbf{Z}_i = (Z_{ix}, Z_{iy}, Z_{iz})$ are complex parameters to denote the centroid of each single-particle wave function in phase space. The complex parameters $\chi_i^{\uparrow}$ and $\chi_i^{\downarrow}$ denote the spin directions. Axial symmetry is not assumed.

2.2. *Energy variation*

Basis wave functions of the GCM are obtained via the energy variation with a constraint potential $V_{\rm cnst}$ after projection onto positive-parity states,

$$\delta\left(\frac{\langle\Phi^+|\hat{H}|\Phi^+\rangle}{\langle\Phi^+|\Phi^+\rangle}+V_{\rm cnst}\right)=0, \tag{6}$$

$$|\Phi^+\rangle=\frac{1+\hat{P}_r}{2}|\Phi\rangle, \tag{7}$$

where $\hat{H}$ is a Hamiltonian, and $\hat{P}_r$ denotes the parity operator. The energy variation is performed by solving time evolution equations,

$$\frac{dX}{dt}=-\mu_X\frac{\partial}{\partial X}\left(\frac{\langle\Phi^+|\hat{H}|\Phi^+\rangle}{\langle\Phi^+|\Phi^+\rangle}+V_{\rm cnst}\right), \tag{8}$$

$$\frac{d\mathsf{K}}{dt}=-\mu_{\mathsf{K}}\frac{\partial}{\partial \mathsf{K}}\left(\frac{\langle\Phi^+|\hat{H}|\Phi^+\rangle}{\langle\Phi^+|\Phi^+\rangle}+V_{\rm cnst}\right), \tag{9}$$

where X denotes a complex parameter, and μ_X and μ_{K} are positive numbers. After a sufficient number of time steps, a local minimum energy state is obtained. In practice, Eq. (9) is solved after a transformation to diagonalize the K matrix. The variational parameters are K, $\mathbf{Z}_i$, and $\chi_i^{\uparrow,\downarrow}$ ($i=1,\ldots,A$). The isospin component of each single-particle wave function is fixed as a proton (π) or a neutron (ν). Initial wave functions are generated randomly. The Gogny D1S force is used as the effective interaction.

To obtain deformed and cluster structure wave functions, two types of constraints $V_{\rm cnst}$ are used: the quadrupole deformation parameter β of the total system and the distance d between α and ^{38}Ar clusters,

$$V_{\rm cnst}=\begin{cases}v_\beta(\beta-\beta_0)^2\\ v_d(d-d_0)^2\end{cases}. \tag{10}$$

Here β is the matter quadrupole deformation parameter. The distance d between α and ^{38}Ar clusters is defined as the distance between the centers of mass of α and ^{38}Ar clusters,

$$d=|\mathbf{R}_{\alpha\text{-}^{38}\rm Ar}|, \tag{11}$$

$$\mathbf{R}_{\alpha\text{-}^{38}\rm Ar}=\left(\frac{1}{4}\sum_{i\in\alpha}-\frac{1}{38}\sum_{i\in{}^{38}\rm Ar}\right)\mathrm{Re}(\mathsf{K}^{-1}\mathbf{Z}_i), \tag{12}$$

where $i\in\alpha$ and ^{38}Ar mean that the ith nucleon is contained in α and ^{38}Ar clusters, respectively. It should be noted that the spatial center of the single-particle wave function $|\varphi_i\rangle$ is $\mathrm{Re}(\mathsf{K}^{-1}\mathbf{Z}_i)$. Details of the constraint of intercluster distance are provided in Ref. [17]. When sufficiently large values are chosen for v_β and v_d, the resultant values β and d become β_0 and d_0, respectively.

2.3. *Generator coordinate method*

After performing the constraint energy variation for $|\Phi^+\rangle$, we superpose the optimized wave functions by employing the quadrupole deformation parameter β and the distances d between α and ^{38}Ar

clusters,

$$\left|\Phi^{J+}_{M}\right\rangle = \sum_{K} \hat{P}^{J\pi}_{MK} \left(\sum_{i} f^{\beta}_{iK} \left|\Phi^{\beta}_{i}\right\rangle + \sum_{i} f^{d}_{iK} \left|\Phi^{d}_{i}\right\rangle \right), \tag{13}$$

where $\hat{P}^{J^\pi}_{MK}$ is the parity and total angular momentum projection operator, and $|\Phi^{\beta}_{i}\rangle$ and $|\Phi^{d}_{i}\rangle$ are optimized wave functions with β and d constraints for the constrained values $\beta = \beta^{(i)}_0$ and $d = d^{(i)}_0$, respectively. The integrals over the three Euler angles in the total angular momentum projection operator $\hat{P}^{J}_{MK}$ are evaluated by numerical integration. The numbers of sampling points in the numerical integration are 23, 27, and 23 for α, β, and γ, respectively. Here the body-fixed x-, y-, and z-axes are chosen as $\langle x^2\rangle \le \langle y^2\rangle \le \langle z^2\rangle$ for $\gamma < 30^\circ$ wave functions and $\langle x^2\rangle \ge \langle y^2\rangle \ge \langle z^2\rangle$ for $\gamma > 30^\circ$ ones in the case of β-constrained wave functions. In the case of d-constrained wave functions, the z-axis is chosen as the vector that connects the α and ^{38}Ar clusters. The coefficients f^{β}_{iK} and f^{d}_{iK} are determined by the Hill–Wheeler equation,

$$\delta\left(\left\langle \Phi^{J+}_{M} \middle| \hat{H} \middle| \Phi^{J+}_{M} \right\rangle - \epsilon \left\langle \Phi^{J+}_{M} \middle| \Phi^{J+}_{M} \right\rangle \right) = 0. \tag{14}$$

Then we get the energy spectra and the corresponding wave functions that are expressed by the superposition of the optimum wave functions, $\{|\Phi^{\beta}_{i}\rangle\}$ and $\{|\Phi^{d}_{i}\rangle\}$.

3. GCM basis obtained by energy variation

Figure 1 shows the energy curves as functions of β, which are obtained by the energy variations with the constraint on β. Harmonic-oscillator (HO) quanta of obtained wave functions for protons and neutrons, N_π and N_ν, respectively, are $(N_\pi, N_\nu) = (0, 0)$, (2, 0), (2, 2), and (4, 2) on and close to the β-energy surface relative to the lowest-allowed state. The N_τ ($\tau = \pi$ or ν) are defined as

$$N_\tau = \left\langle \sum_{i\in\tau} \left[\frac{1}{2}(\mathsf{K}\hat{\mathbf{r}}_i)^2 + \frac{1}{2}\left(\mathsf{K}^{-\mathrm{T}}\hat{\mathbf{k}}_i\right)^2 \right] \right\rangle - \frac{3}{2}n_\tau - N_{0\tau}, \tag{15}$$

where n_π and n_ν denote proton and neutron numbers, respectively, and $N_{0\pi}$ and $N_{0\nu}$ denote HO quanta of the lowest-allowed states for protons and neutrons, respectively. The (0, 0), (2, 0), (2, 2), and (4, 2) configurations correspond to configurations of $[(pf)^2]_\nu$, $[(sd)^{-2}(pf)^2]_\pi[(pf)^2]_\nu$, $[(sd)^{-2}(pf)^2]_\pi[(sd)^{-2}(pf)^4]_\nu$, and $[(sd)^{-4}(pf)^4]_\pi[(sd)^{-2}(pf)^4]_\nu$, respectively, which in total are the $2p$, $4p2h$, $6p4h$, and $8p6h$ configurations, respectively. The $4p2h$, $6p4h$, and $8p6h$ states have local minima at $\beta \sim 0.3$, 0.4, and 0.5, respectively. Deformations of the protons and neutrons are similar across the whole β region. The $4p2h$, $6p4h$, and $8p6h$ states form triaxially deformed structures. Several wave functions that differ in their particle–hole configurations are obtained in a common β value, which are at local minima on the energy-surface plane with a constraint on the β value. In practice, they are obtained by two steps. First, initial wave functions of the energy variation are generated randomly, and optimized wave functions are obtained for each deformation parameter β. Second, the optimized wave functions are set to initial wave functions for different β values. Density distributions of the wave functions at local minima with $2p$, $4p2h$, $6p4h$, and $8p4h$ configurations are shown in Figs. 2(a)–(d), respectively; these distributions do not have significant neck structures.

Through the AMP, largely deformed states gain higher binding energies, and the energy of the local-minimum state for the $6p4h$ configuration projected onto the $J^\pi = 0^+$ state becomes lower than that for the $4p2h$ configuration. The order of the local-minimum energies is the reverse of that before the AMP.

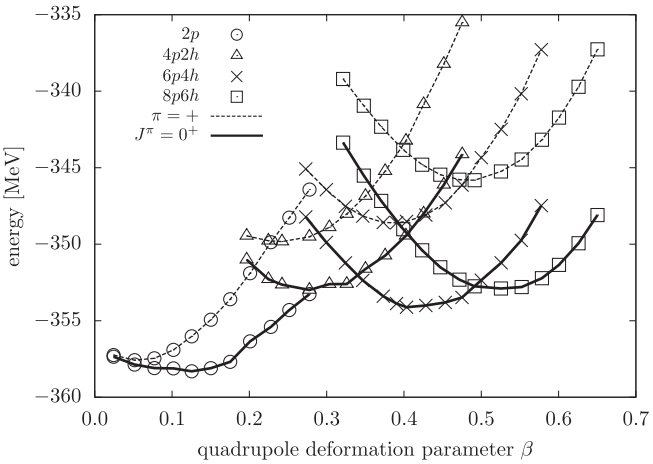

Fig. 1. The energy curves as functions of the quadrupole deformation parameter β for positive-parity (dashed lines) and $J^\pi = 0^+$ (solid lines) states. Circles, triangles, crosses, and squares indicate the $2p$, $4p2h$, $6p4h$, and $8p6h$ configurations, respectively (see text).

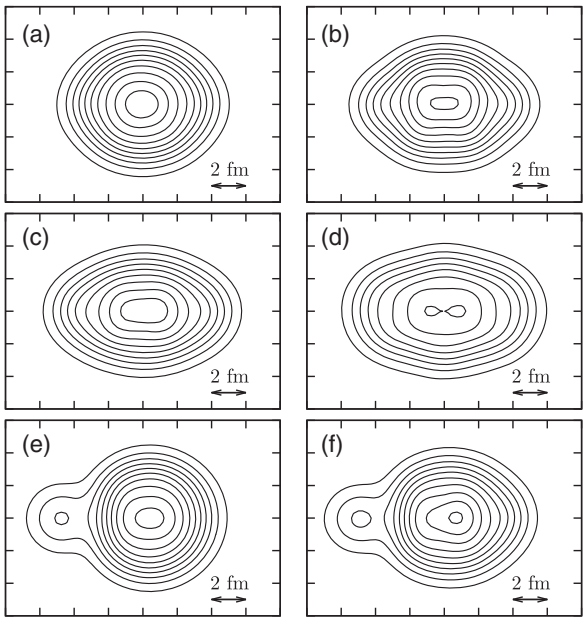

Fig. 2. Density distributions of (a) $2p$ ($\beta = 0.13$), (b) $4p2h$ ($\beta = 0.28$), (c) $6p4h$ ($\beta = 0.43$), and (d) $8p6h$ ($\beta = 0.53$) wave functions obtained with the quadrupole deformation parameter β constraint, and (e) A- and (f) B-type wave functions obtained with the intercluster distance constraint ($d = 5.0$ fm).

The upper panel of Fig. 3 shows energy curves of α–^{38}Ar cluster structures as functions of intercluster distance between α and ^{38}Ar clusters obtained by energy variations with the α–^{38}Ar intercluster-distance constraint. In the calculations, two types, called A and B types, of α–^{38}Ar cluster structure wave functions are obtained that differ in the orientation of the ^{38}Ar clusters. An ^{38}Ar cluster has a two proton-hole configuration relative to the sd-shell double-closed structure. Proton holes of ^{38}Ar clusters in A- and B-type wave functions are in parallel and orthogonal directions to an α cluster, respectively. In the small intercluster-distance region, the A type has similar energies to the minimum energy on the β-energy surface. But the B type is still excited, and the energies are similar to those at the local minimum of the $4p2h$ configuration of β-energy curves. The lower

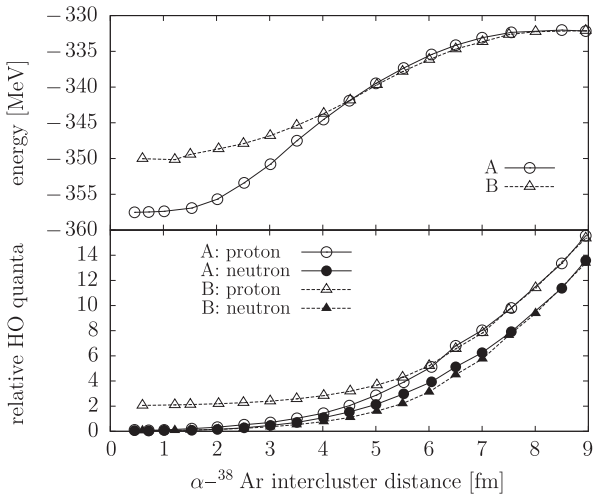

Fig. 3. (Upper) Solid and dashed curves show energies of α–^{38}Ar cluster structures for A and B types (see text), respectively, as functions of intercluster distance. (Lower) Solid and dashed curves show harmonic oscillator quanta for A and B types (see text), respectively, relative to the lowest-allowed state in ^{42}Ca as functions of intercluster distance. Open and closed symbols are for protons and neutrons, respectively.

panel of Fig. 3 shows HO quanta for protons and neutrons, respectively, relative to the lowest-allowed state in ^{42}Ca. At small intercluster distance, the A type goes to the lowest-allowed state, whereas the proton parts of the B type are $2\hbar\omega$ excited, which is the $4p2h$ configuration. This is because protons on the direction of an α cluster are occupied in the sd-shell in the B-type ^{38}Ar clusters. Owing to the Pauli principle, two protons are in the pf-shell even at small α–^{38}Ar intercluster distances. Density distributions of A- and B-type wave functions with $d = 5.0$ fm are shown in Figs. 2(e) and (f), respectively. They have two spatially localized subsystems corresponding to α and ^{38}Ar clusters, which show α–^{38}Ar cluster structures. The shapes of the ^{38}Ar clusters are distorted due to intercluster interaction, although the ground state of ^{38}Ar is almost spherical.

4. Coexistence of various rotational bands

4.1. Level scheme

Figure 4 shows the level scheme of the positive-parity states in ^{42}Ca up to the $J^\pi = 8^+$ states obtained via the AMP and the GCM. The GCM bases are deformed-structure wave functions with configurations of $2p$, $4p2h$, $6p4h$, and $8p6h$ obtained via energy variations with the β constraint and the α–^{38}Ar cluster structure wave functions obtained via energy variations with the α–^{38}Ar intercluster-distance constraint set to a maximum of 9.0 fm. Wave functions that contain more than 0.5% of the J^+K components $\langle \hat{P}^{J+}_{KK} \rangle$ are adopted in the GCM basis for each JK to avoid numerical errors in the AMP. The convergence of the GCM calculation was confirmed by a comparison with a restricted set of basis wave functions (the energies of the states listed in Fig. 4 change by less than 0.3 MeV when the number of basis wave functions is halved). Three $K^\pi = 0^+$ rotational bands coexist in the excited states, called ND1, ND2, and SD.

Figure 5 shows squared overlaps of the $J^\pi = 0^+$ states and the $J^\pi = 0^+$ components of wave functions obtained by energy variation with the β constraint for the GS, ND1, ND2, and SD bands. The dominant components of the ND1, ND2, and SD states have $6p4h$, $4p2h$, and $8p6h$ configurations, respectively, and the quadrupole deformation parameters of their dominant components are

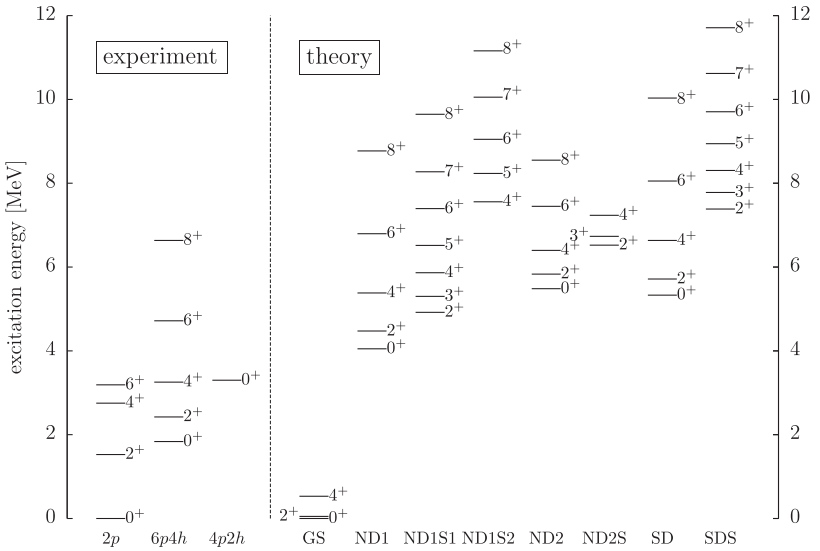

Fig. 4. The experimental and theoretical level schemes in ^{42}Ca.

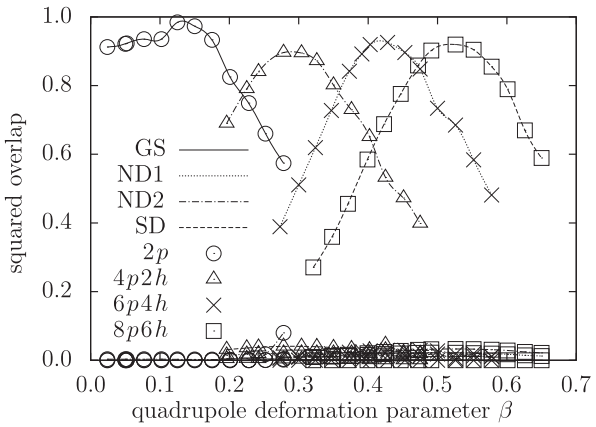

Fig. 5. Squared overlaps of $J^\pi = 0^+$ states in the GS (solid), ND1 (dotted), ND2 (dot-dashed), and SD bands (dashed), and $J^\pi = 0^+$ components of wave functions obtained by energy variation with the β constraint. Circle, triangle, cross, and square symbols are for the $2p$, $4p2h$, $6p4h$, and $8p6h$ wave functions, respectively.

$\beta = 0.43$, 0.28, and 0.53, respectively. The ground-state (GS) band has a $2p$ configuration. The theoretical level spacings of the GS band are underestimated, although the GS band is considered to have a simple $[(f_{7/2})^2]_\nu$ structure. This underestimation does not affect the qualitative properties of the ND1, ND2, and SD bands because the particle–hole configurations of their dominant components are very different from those of the GS band. The underestimation may be caused by insufficient treatment of the pairing effect. In the present study, the pairing effect is not taken into account directly, although the effects are in principle included by superposition of wave functions. In some GCM bases, time-reversal symmetry is broken since it is not assumed in the present framework. But the level scheme does not change when time-reversal pair wave functions are adopted in the GCM basis, which means that time-reversal symmetry is restored by the AMP and GCM.

The present results suggest the existence of side bands of the ND1, ND2, and SD bands due to triaxial deformation. ND1S1 and ND1S2 are side bands of the ND1 band whose dominant K components are $|K| = 2$ and 4, respectively. The ND2S and SDS bands are side bands of the ND2 and

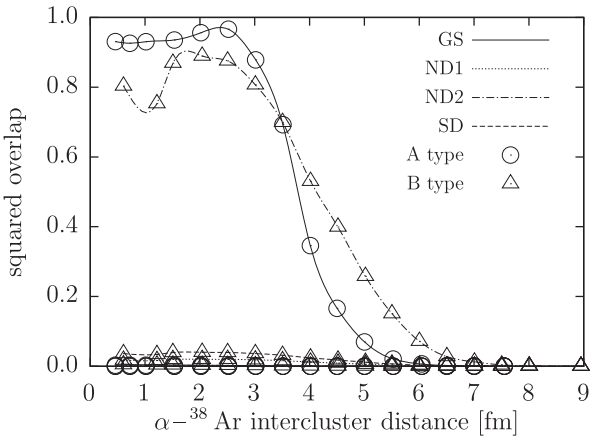

Fig. 6. Squared overlaps of the $J^\pi = 0^+_{\rm GS}$ (solid), $0^+_{\rm ND1}$ (dotted), $0^+_{\rm ND2}$ (dot-dashed), and $0^+_{\rm SD}$ (dashed) states and the α–^{38}Ar cluster structure wave functions as functions of the distance between α and ^{38}Ar clusters. Open and closed symbols are for A- and B-type wave functions, respectively.

SD bands, respectively, with dominant components of $|K| = 2$. The ND2 and SD bands, and the side bands of the ND1, ND2, and SD bands, are theoretical predictions; candidate states have not yet been observed.

4.2. α–^{38}Ar cluster correlations

To analyze the α–^{38}Ar cluster structure correlations in the low-lying rotational bands, squared overlaps of the band-head states and α–^{38}Ar cluster structure components were calculated for the GS, ND1, ND2, and SD bands, as shown in Fig. 6. The $J^\pi = 0^+_{\rm GS}$ and $0^+_{\rm ND2}$ states have a large amount of A- and B-type α–^{38}Ar cluster structure components, respectively, at large intercluster distances as well as at small distances. The particle–hole configurations of the A- and B-type α–^{38}Ar cluster structure wave functions are equal to the the dominant particle–hole configurations of the $J^\pi = 0^+_{\rm GS}$ and $0^+_{\rm ND2}$ states, respectively, in the small intercluster-distance region, which shows that the particle–hole configurations of cluster wave functions at small intercluster distances are important for coupling to deformed states. The $J^\pi = 0^+_{\rm ND1}$ and $0^+_{\rm SD}$ states have a small amount of α–^{38}Ar cluster structure components for any intercluster distance. The distributions of squared overlaps are similar up to the high-spin state in each band.

4.3. E2 transition strengths

The B(E2) values of the in-band transitions in the theoretical ND1, ND2, and SD bands and the experimental $K^\pi = 0^+_2$ band in Weisskopf units are listed in Table 1. The theoretical values for the ND1 band are within the error of the experimental values for the $K^\pi = 0^+_2$ band. The in-band B(E2) values from the higher-spin state of the ND2 band are smaller, which is caused by mixing of components other than the $4p2h$ configuration in higher-spin states. The B(E2) values of the SD band are much larger than those of the ND1 and ND2 bands.

4.4. Band assignment

The amount of α–^{38}Ar cluster components (Fig. 6), particle–hole configurations of dominant components, and the in-band transition B(E2) values (Table 1) indicate that the ND1 band and the ND2 band head correspond to the experimental $K^\pi = 0^+_2$ band and $J^\pi = 0^+_3$ state, respectively. The large

Table 1. Theoretical and experimental B(E2) values in Weisskopf units $B_{\mathrm{W.u.}} = 8.67\ \mathrm{e}^2\,\mathrm{fm}^4$ (I_i and I_f indicate initial and final states, respectively). Experimental values are taken from Refs. [5,18].

	I_i	I_f	B(E2)
theory	2^+_{ND1}	0^+_{ND1}	28.55
	4^+_{ND1}	2^+_{ND1}	33.12
	6^+_{ND1}	4^+_{ND1}	38.45
	2^+_{ND2}	0^+_{ND2}	29.02
	4^+_{ND2}	2^+_{ND2}	24.70
	6^+_{ND2}	4^+_{ND2}	24.61
	2^+_{SD}	0^+_{SD}	82.12
	4^+_{SD}	2^+_{SD}	107.99
	6^+_{SD}	4^+_{SD}	130.18
experiment	4^+_2	2^+_2	57 ± 42
($K^\pi = 0^+_2$ band)	6^+_2	4^+_2	50^{+35}_{-16}

amount of α–^{38}Ar cluster components in the $J^\pi = 0^+_{\mathrm{ND2}}$ state reveals that this state corresponds to the experimental $J^\pi = 0^+_3$ state because of strong populations to the $J^\pi = 0^+_3$ state by α-transfer reactions to ^{38}Ar [13], which are sensitive to α–^{38}Ar cluster structure components. The ND1 states have a small amount of α–^{38}Ar cluster structure components and similar in-band B(E2) values to those of the experimental $K^\pi = 0^+_2$ band, which indicates that the ND1 band corresponds to the experimental $K^\pi = 0^+_2$ band. The particle–hole configurations of the ND1 ($6p4h$) and ND2 ($4p2h$) bands are consistent with those of the $J^\pi = 0^+_2$ and 0^+_3 states, respectively, suggested by the results of an α-transfer experiment [13]. The members of the ND2 band apart from the band head and those of the SD band have not yet been observed. The members of the ND2 band could possibly be observed by a combination of α-transfer reactions and γ-spectroscopy experiments, because the ND2 band contains a large amount of α–^{38}Ar cluster structure components and has large in-band B(E2) values.

This full-microscopic model reveals the coexistence of three low-lying rotational $K^\pi = 0^+$ bands with $6p4h$, $4p2h$, and $8p6h$ configurations in ^{42}Ca, but the α + ^{38}Ar OCM, which is a semi-microscopic model, produces only one $K^\pi = 0^+$ rotational band with a $4p2h$ configuration in the low-lying states. Full-microscopic models treating clustering and various deformations with mp–mh configurations are required to understand the low-lying structures in ^{42}Ca. A unified treatment of clustering and deformation is important for studying nuclear structures.

5. Particle–hole configurations and E2 transitions

The in-band B(E2) values, deformations, and particle–hole configurations in the ND1 and ND2 bands found here indicate that the in-band B(E2) values are more sensitive to the proton particle–hole configurations than to deformations, which are not necessarily related to the B(E2) values. Indeed, for ND1 and ND2 bands with the same proton particle–hole configurations, $(sd)^{-2}(pf)^2$, the calculated in-band B(E2) values are similar although their dominant components have different quadrupole deformations of $\beta = 0.40$ and 0.28, respectively. This is inconsistent with a simple collective model in which the B(E2) values are proportional to β^2. Experimental B(E2) values of the in-band transitions in the ND band in ^{40}Ca, whose proton particle–hole configurations are also $(sd)^{-2}(pf)^2$, are similar to the theoretical B(E2) values of the ND1 and ND2 bands in ^{42}Ca. As the Nilsson orbits

show, particle–hole configurations are strongly related to deformation, but a careful consideration of both the particle–hole configurations and deformation are required for understanding the structures of deformed states.

6. Conclusions

In conclusion, the structures of the deformed states in ^{42}Ca have been investigated using deformed-basis AMD and the GCM by focusing on the coexistence of various rotational bands with mp–mh configurations and α–^{38}Ar clustering. In the excited states, three $K^\pi = 0^+$ bands, ND1, ND2, and SD, are obtained, which have dominant $6p4h$, $4p2h$, and $8p6h$ configurations, respectively. The ND1 band corresponds to the experimental $K^\pi = 0^+_2$ band, while the ND2 and SD bands have not yet been observed. The band head of the ND2 band corresponds to the experimental $J^\pi = 0^+_3$ state. The B(E2) values of the in-band transitions of the ND1 band are consistent with experimental data. The members of the GS and ND2 bands contain a large amount of α–^{38}Ar cluster structure components, which is consistent with results that show that the $J^\pi = 0^+_1$ and 0^+_3 states are strongly populated by ^{38}Ar(^{6}Li, d) reactions. Particle–hole configurations of the dominant components of the GS and ND2 bands are consistent with the suggestions of the α-transfer to ^{38}Ar experiment. E2 transitions are more sensitive to proton particle–hole configurations than to deformation. It is necessary to employ full-microscopic calculations and consider both clustering and various deformations with mp–mh configurations to understand the low-lying states in ^{42}Ca.

Acknowledgements

The author thanks Dr Y. Kanada-En'yo and Dr M. Kimura for careful proofreading and valuable comments. Thanks are also given to Prof. H. Horiuchi, Prof. K. Ikeda, Dr E. Ideguchi, and Dr M. Niikura for fruitful discussions. This work was supported by JSPS KAKENHI Grant Number 25800124 and the University of Tsukuba Research Infrastructure Support Program. Numerical calculations were conducted on the T2K-Tsukuba at the Center for Computational Sciences, University of Tsukuba and the RIKEN Integrated Cluster of Clusters (RICC).

References

[1] C. E. Svensson, A. O. Macchiavelli, A. Juodagalvis, A. Poves, I. Ragnarsson, S. Åberg, D. E. Appelbe, R. A. E. Austin, G. C. Ball, M. P. Carpenter, E. Caurier, R. M. Clark, M. Cromaz, M. A. Deleplanque, R. M. Diamond, P. Fallon, R. V. F. Janssens, G. J. Lane, I. Y. Lee, F. Nowacki, D. G. Sarantites, F. S. Stephens, K. Vetter, and D. Ward, Phys. Rev. C, **63**, 061301 (2001).
[2] D. Rudolph, A. Poves, C. Baktash, R. A. E. Austin, J. Eberth, D. Haslip, D. R. LaFosse, M. Lipoglavšek, S. D. Paul, D. G. Sarantites, C. E. Svensson, H. G. Thomas, J. C. Waddington, W. Weintraub, and J. N. Wilson, Phys. Rev. C, **65**, 034305 (2002).
[3] E. Ideguchi, S. Ota, T. Morikawa, M. Oshima, M. Koizumi, Y. Toh, A. Kimura, H. Harada, K. Furutaka, S. Nakamura, F. Kitatani, Y. Hatsukawa, T. Shizuma, M. Sugawara, H. Miyatake, Y. X. Watanabe, Y. Hirayama, and M. Oi, Phys. Lett. B, **686**, 18 (2010).
[4] E. Ideguchi, D. G. Sarantites, W. Reviol, A. V. Afanasjev, M. Devlin, C. Baktash, R. V. F. Janssens, D. Rudolph, A. Axelsson, M. P. Carpenter, A. Galindo-Uribarri, D. R. LaFosse, T. Lauritsen, F. Lerma, C. J. Lister, P. Reiter, D. Seweryniak, M. Weiszflog, and J. N. Wilson, Phys. Rev. Lett., **87**, 222501 (2001).
[5] P. Betz, E. Bitterwolf, B. Busshardt, and H. Röpke, Z. Phys. A, **276**, 295 (1976).
[6] M. Lach, J. Styczen, W. Meczynski, P. Bednarczyk, A. Bracco, J. Grebosz, A. Maj, J. C. Merdinger, N. Schulz, M. B. Smith, K. M. Spohr, J. P. Vivien, and M. Zieblinski, Eur. Phys. J. A, **16**, 309 (2003).
[7] C. D. O'Leary, M. A. Bentley, B. A. Brown, D. E. Appelbe, R. A. Bark, D. M. Cullen, S. Ertürk, A. Maj, and A. C. Merchant, Phys. Rev. C, **61**, 064314 (2000).
[8] F. Michel, S. Ohkubo, and G. Reidemeister, Prog. Theor. Phys. Suppl., **132**, 7 (1998), and references therein.

[9] T. Yamaya, K. Katori, M. Fujiwara, S. Kato, and S. Ohkubo, Prog. Theor. Phys. Suppl., **132**, 73 (1998), and references therein.
[10] T. Sakuda and S. Ohkubo, Prog. Theor. Phys. Suppl., **132**, 103 (1998), and references therein.
[11] Y. Taniguchi, M. Kimura, Y. Kanada-En'yo, and H. Horiuchi, Phys. Rev. C, **76**, 044317 (2007).
[12] M. Kimura and H. Horiuchi, Nucl. Phys. A, **767**, 58 (2006).
[13] H. T. Fortune, R. R. Betts, J. N. Bishop, M. N. I. Al-Jadir, and R. Middleton, Nucl. Phys. A, **294**, 208 (1978).
[14] T. Sakuda and S. Ohkubo, Phys. Rev. C, **51**, 586 (1995).
[15] Y. Kanada-En'yo and H. Horiuchi, Prog. Theor. Phys., **93**, 115 (1995).
[16] M. Kimura, Phys. Rev. C, **69**, 044319 (2004).
[17] Y. Taniguchi, M. Kimura, and H. Horiuchi, Prog. Theor. Phys., **112**, 475 (2004).
[18] J. A. Cameron and B. Singh, Nucl. Data Sheets, **102**, 293 (2004).